Materials Today Bio 32 (2025) 101869

Contents lists available at ScienceDirect

Materials Today Bio

journal homepage: www.journals.elsevier.com/materials-today-bio

Highly efficient NIR-II photothermal therapy amplified ROS oxide breast tumor therapy by mesoporous gallium-enriched platinum nanomedicine

Yunfei Ying [a,b,1], Yonghui Su [a,d,1], Ao Wang [a,b,e], Tingting Li [a,b], Hongjun Zhuang [a,d], Siyaqi Li [a], Xiaolong Liu [b,c], Kecan Lin [c,*], Peiyuan Wang [a,b,**], Fuxing Zhang [a,***]

[a] Department of General Surgery, The First Hospital Affiliated to Xiamen University, School of Medicine, Xiamen University, Xiamen, 361004, PR China
[b] Key Laboratory of Design and Assembly of Functional Nanostructures, Fujian Institute of Research on the Structure of Matter, Chinese Academy of Sciences, Fuzhou, 350002, PR China
[c] The United Innovation of Mengchao Hepatobiliary Technology Key Laboratory of Fujian Province, Mengchao Hepatobiliary Hospital of Fujian Medical University, Fuzhou, 350025, PR China
[d] Department of Breast Surgery, The First Affiliated Hospital of Xiamen University, School of Medicine, Xiamen University, Xiamen, 361003, PR China
[e] Department of Medical Imaging Technology, College of Medical Technology and Engineering, Fujian Medical University, Fuzhou, 350122, PR China

ARTICLE INFO

Keywords:
Mesoporous structure
PtGaP nanomedicine
Tumor targeting
NIR-II PTT
Synergistic OXT

ABSTRACT

Rational design and exploitation of nanomaterials with superior treatment properties for suitable indications is a way out to relieve cost constraint of therapy and solve the unsatisfactory efficacy for cancer patients. In this work, in order solve the current bottleneck problems of photothermal therapy (PTT) with longer light excitation as well as synergistic eactive oxygen species (ROS) storm mediating *via* mental element catalyst without toxic side effects. We have proposed a one-step method to produce mesoporous PtGa bimetallic composition with surface modification of PEG_{2000} (PtGaP) for the first time. Specifically, it can effectively concentrate at tumor tissues *via* the mesoporous nanostructure. Owing to the strong absorption in NIR-II region (1000–1700 nm) from Pt and Fenton-like catalyst of Ga, the ROS storm is efficaciously mediated. Remarkably, under safer NIR-II (1064 nm) laser irradiation, both *in vitro* and *in vivo* studies confirm that our bimetallic mesoporous nanomedicine effectively prevents tumor growth through synergistic PTT and oxidative therapy (OXT). Given its high bio-safety performance, we can conclude that the PtGaP has strong biocompatibility and holds great prospect in clinic translation.

1. Introduction

In 2023, breast cancer accounted for 31 % of all cancer cases and 15 % of cancer-related deaths among women in the United States, making it the most prevalent cancer worldwide [1]. Treatment options for breast cancer include breast-conserving surgery and mastectomy, followed by chemotherapy or radiotherapy to reduce the likelihood of recurrence [2,3]. However, the long-term side effects of chemotherapy [4–6] and the toxicity associated with radiotherapy [7] pose significant limitations. Preoperative therapies, which can convert inoperable tumors into operable ones, offer potential for de-escalating treatment and improving outcomes [7,8]. These therapies include anticancer nanoparticles [9], immunotherapy [10], targeted therapies [11], and antibody-drug conjugates [12]. Functional anticancer nanoparticles can generate reactive oxygen species (ROS) in the tumor environment, ultimately leading to cancer cell death [13–18]. Gallium (Ga) is a trace element in the human body that exists in a trivalent form, which shares many properties with iron (Fe), such as ionic radius, ionization potential, and electron affinity [19]. Because of these chemical similarities, biological systems often cannot distinguish between Fe^{III} and Ga^{III}, allowing Ga^{III} to replace Fe^{III} in the active centers of proteins involved in iron metabolism, which can disrupt their normal functions [20]. This unique characteristic of Ga^{III} has led to its use in several FDA-approved treatments, such as Ga-68 for positron emission tomography (PET) imaging, Ga-67 citrates for

* Corresponding author.
** Corresponding author. Department of General Surgery, The First Hospital Affiliated to Xiamen University, School of Medicine, Xiamen University, Xiamen, 361004, PR China.
*** Corresponding author.
E-mail addresses: kclin2002@126.com (K. Lin), wangpeiyuan@fjirsm.ac.cn (P. Wang), fuxingzhang@xmu.edu.cn (F. Zhang).
[1] These authors contributed equally to this work.

https://doi.org/10.1016/j.mtbio.2025.101869
Received 8 March 2025; Received in revised form 8 May 2025; Accepted 12 May 2025
Available online 13 May 2025

diagnostic radiotherapy, and injectable gallium nitrate ($Ga(NO_3)_3$) for treating hypercalcemia [21–24]. Additionally, a formulation of Ga, Ga maltolate, is currently in clinical trials [25], demonstrating its growing potential in biomedical applications. Despite its clinical benefits, Ga^{III} may form gallium hydroxide ($Ga(OH)_3$) under physiological conditions, which has low solubility and bioavailability, thus limiting its therapeutic effectiveness [26]. Moreover, direct exposure to free Ga^{III} can lead to toxic side effects, such as nephrotoxicity, renal acidosis, and glomerular damage [27,28].

Ga^{II}, similar to Fe^{II}, can serve as a Fenton reagent to induce oxidative therapy (OXT) by generating reactive oxygen species (ROS) in tumor cells. However, due to the lack of specificity during circulation in the bloodstream, Ga^{II} carriers may undergo premature bio-oxidation, driven by the relatively low redox potential of the Ga^{III}/Ga^{II} couple [29]. This can lead to excessive H_2O_2 production and cause adverse effects in healthy tissues, especially under conditions like lipopolysaccharide-induced inflammation [30,31]. To address this issue, researchers have turned to amorphous Ga^0 nanoparticles, which are designed to rapidly ionize in the acidic tumor microenvironment, releasing Ga^{II} on demand. This enables a localized Fenton like reaction, providing a more targeted approach for cancer treatment [32]. The stimulus-responsive nature of this system makes the therapy more specific to the tumor site. While OXT alone is often insufficient for optimal therapeutic outcomes, combining it with other treatments is frequently necessary for better results [33–35]. Synergistic therapy has been widely used in tumor inhibition [36–40]. Based on the collision theory of thermodynamic molecules, increasing the local temperature could improve the efficiency of the Fenton reaction [41–44], making photothermal therapy (PTT) an ideal complementary treatment [45–47]. Platinum (Pt) nanoparticles are particularly well-suited for PTT due to their excellent longitudinal surface plasmon resonance, resistance to photobleaching, and biocompatibility *in vivo*, particularly in the NIR-II range (1000–1700 nm) [48–54]. Therefore, developing and optimizing Ga and Pt co-doped nanoparticles holds significant promise for breast cancer treatment. This approach, combining two FDA-approved components, is crucial for advancing the clinical application of nanomedicine.

Bearing the above critical issues, we have adopted a one step to prepare Pt and Ga^0 bimetallic co-doped composition (PtGa) assembled by spatially interconnected in high yield by a simple ultrasonic treatment of reaction at room temperature, using K_2PtCl_4 and $GaCl_3$ as the raw precursors. This effectively simplified and the preparation process and reduced unsuspected interferential factors to achieve repeatable structural and functional optimization. Additionally, the unique mesoporous nanostructure of PtGa is a promising Fenton like catalyst due to their higher surface area with more exposure active site relative to their solid counterparts. PEG_{2000} motifs are subsequently grafted on surface (PtGaP), this nanoplatform can efficaciously accumulated in the breast tumor regions, interestingly, upon NIR-II (1064 nm) laser irradiation, high photothermal-conversion efficiency of the nanomedicine is demonstrated, then the local thermal progressively potentiates ROS amplification *via* the catalyst of Ga^0. Both *in vitro* and *in vivo* studies demonstrate that our bimetallic mesoporous nanomedicine is able to efficaciously prevent tumorigenesis *via* synergistic PTT & OXT (Fig. 1). All findings highlight the potency of Pt and Ga based nanocomposites as chemodynamic nanoagents for malignant breast cancer ablating *via* synergistic effect accompanied by NIR-II light illumination.

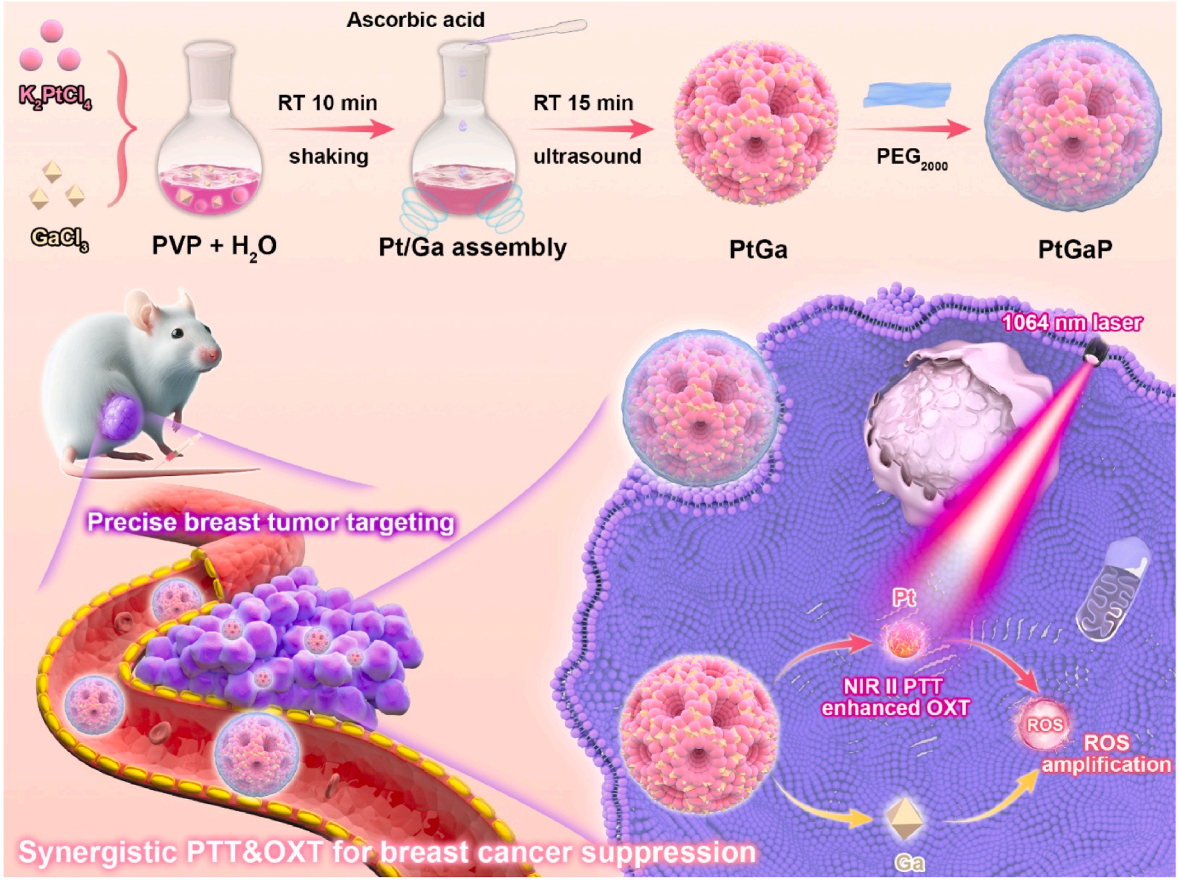

Fig. 1. One-step synthesis of mesoporous bimetallic PtGa nanocrystals with precise breast tumor targeting and ablating *via* synergistic PTT and OXT under 1064 nm laser irradiation.

2. Materials and method

2.1. PtGa fabrication

PtGa nanocomposites were usually fabricated by preparing a 1 mL aqueous mixture consisting of 0.3 mL of a 20 mM solution of Ga $(NO_3)_3$•$6H_2O$, 0.7 mL of a 20 mM solution of K_2PtCl_4, and 0.01 g of poly (vinylpyrrolidone) (PVP). Subsequently, 1 mL of a 0.1 M ascorbic acid (AA) solution was rapidly introduced into the mixture. The resulting solution was then sonicated for 15 min at ambient temperature. The PtGa nanocrystals were isolated by centrifugation at 10000 rpm for 20 min, and this process was repeated three times with water to ensure thorough washing. The purified product was subsequently stored for subsequent analysis.

2.2. PtGaP synthesis

A PEGylated surface modification of PtGa (denoted as PtGaP) was achieved by combining 100 mg of PtGa nanoparticles with 25 mg of PEG_{2000} in 10 mL deionized water. The mixture underwent12-h homogenization through continuous gentle agitation at ambient temperature. Subsequent purification involved three centrifugation cycles (15,000 rpm, 30 min each) to eliminate unbound PEG_{2000} molecules. The final PtGaP product was isolated through centrifugal separation and subsequently redispersed in fresh deionized water (10 mL) for colloidal stabilization.

2.3. PtGaP@I fabrication

ICG powder (1 mg) was initially dissolved in 3 mL of absolute alcohol. Subsequently, 30 mL of the synthesized PtGaP nanoparticles were promptly introduced into the ICG/ethanol solution. The mixture of PtGaP and ICG was stirred continuously at a temperature of 37 °C within a dimethyl silicone oil bath for a duration of at least 48 h. Consequently, the ICG was effectively encapsulated within the formed mesopores of the PtGaP nanoparticles during the stirring process. The resulting PtGaP nanoparticles encapsulated with ICG (referred to as PtGaP@I) were then subjected to centrifugal washing with deionized water for 10 min at a speed of 5000 revolutions per minute, a process that was repeated more than thrice. The final step involved drying the PtGaP@I sample under vacuum conditions at a temperature of 60 °C overnight.

2.4. Cytoplasmic ROS detection

Intracellular ROS generation through PtGaP-mediated Fenton like reactions was investigated using confocal laser scanning microscopy (CLSM). Mouse-breast cancer cells (4T1) (1×10^5/well in 6-well plates) were maintained in DMEM supplemented with 10 % FBS and antibiotics. Following 24-h culture, eight experimental cohorts were established: (1) Control, (2) PBS + Laser, (3) H_2O_2, (4) GaP, (5) PtGaP, (6) PtGaP + H_2O_2, (7) PtGaP + Laser, (8) PtGaP + H_2O_2 + Laser. The concentration of H_2O_2 was set as 2 mg/L in all cell studies. After 4-h nanoparticle incubation, designated groups underwent 1064 nm photo-stimulation (1W/cm^2, 5 min). ROS quantification employed DCFH-DA fluorescent probe, with CLSM imaging conducted under standardized parameters (ex/em: 488/525 nm).

2.5. Mitochondrial membrane staining by JC-1

Mitochondrial membrane potentialdepolarization *via* hydroxyl radical were evaluated using JC-1 fluorescence staining. 4T1 carcinoma cells (1×10^5/well) were cultured in 6-well plates for 24 h before randomization into eight treatment cohorts: (1) Control, (2) PBS + Laser, (3) H_2O_2, (4) GaP, (5) PtGaP, (6) PtGaP + H_2O_2, (7) PtGaP + Laser, (8) PtGaP + H_2O_2 + Laser. Following 4-h nanoparticle exposure, designated groups with laser irradiation underwent 1064 nm light stimulation (1W/cm^2, 5 min). JC-1 aggregates (red fluorescence: Ex/Em 530/590 nm) and monomers (green fluorescence: Ex/Em 488/530 nm) were quantified *via* spectral separation, with depolarization ratios calculated from fluorescence intensity differentials.

2.6. NIR-II fluorescent bioimaging for lung tumor recognizing evaluation

All experimental protocols involving vertebrate animals received prior approval from Xiamen University's Ethics Committee. Six-week-old female BALB/c nude mice (Jicui Laboratory Animal Co., Guangzhou) underwent subcutaneous implantation of 4T1 breast carcinoma cells (2×10^6 cells in 200 μL PBS) into right hindlimbs, developing measurable tumors (100–200 mm^3) within 14 days. Test groups (n = 5) received intravenous injections of either free ICG or PtGaP@I nanocomplex (equivalent ICG dosage) for comparative analysis. *In vivo* NIR-II fluorescence imaging was performed at multiple post-administration intervals using a specialized small animal imaging system. Terminal procedures at 48 h post-injection enabled organ/tumor harvest for *ex vivo* fluorescence mapping. Concurrent thermal imaging captured tumor-specific hyperthermia during peak accumulation phases (maximum tumor-to-background ratio, TNR). Both two groups received identical formulations followed by 1064 nm laser exposure (1 W/cm^2, 5 min) at 48 h post-injection. Real-time thermographic monitoring utilized an FOTRIC 225 infrared (IR) camera with calibrated detection parameters. All experimental timelines maintained consistent administration-to-imaging intervals across comparative groups.

2.7. In vivo breast tumor ablation appraising

Subcutaneous breast tumor-bearing BALB/c nude mice (tumor volume ~100 mm^3) were divided into four cohorts (n = 4): 1) PBS control, 2) PBS + Laser (L), 3) PtGaP nanoparticles, and 4) PtGaP + L. Mice received intravenous injections of respective formulations on days 0 and 7, with PtGaP administered at 8.6 mg/kg. Tumor ablation efficacy was assessed post-treatment, with 1064 nm laser irradiation (1 W/cm^2) applied for 5 min at 48 h post-injection. Photographic documentation of all mice was conducted on days 0, 6, and 15. Tumor dimensions (length/width) were measured using digital calipers, with volumes calculated as (width^2 × length)/2. Body weights were monitored triweekly throughout the study. After 15 days of treatment, excised tumors underwent histological processing involving fixation, dehydration, paraffin embedding, and sectioning (10-μm slices). Tissue sections underwent H&E, Ki67, and TUNEL staining for pathological evaluation. Concurrent systemic toxicity assessment was performed through H&E analysis of major organs (cardiac, hepatic, splenic, pulmonary, and renal tissues) following the experimental timeline. Laser irradiation parameters remained constant across applicable groups, while control cohorts received equivalent administration schedules without therapeutic agents or light activation.

2.8. Statistical analysis

Statistical evaluations were conducted using IBM SPSS Statistics. For comparisons involving two groups, a Student's t-test was applied, whereas one-way ANOVA was utilized for analyzing differences among multiple groups. Results are expressed as "mean ± standard deviation (SD)," and statistical significance was defined as $p < 0.01$ (**).

3. Results and discussion

3.1. Mesoporous PtGaP fabrication

Mesoprous PtGa nanoparticles are prepared by one-step solution-phase reaction without the need for high temperature and organic solvent. They are successfully synthesized with the amphiphilic surfactant of PVP, metal co-precursors of K_2PtCl_4 and $GaCl_3$, and the reducing

agent of AA at room temperature. Fig. 2A reveals that the PtGa nanoparticles are well-dispersed with the average size of 20 nm in a high yield. We also detect the size of PtGa to be approximately 21.2 nm through dynamic light scattering (DLS), which is consistent with the results observed *via* TEM images (Fig. S1). Owing to the unique mesoporous nanostructure, the Brunauer-Emmett-Teller (BET) specific surface area of PtGa is determined as 383.2 cm^3/g through nitrogen adsorption-desorption isotherms (Fig. S2). In order to enable prolonged blood circulation time, surface PEGylation is conducted (PtGaP). It is precisely due to the unique mesoporous nanostructure with large specific surface area that PEG_{2000} molecules can be physically adsorbed onto the surface of PtGa. In comparison with PtGa, transmission electron

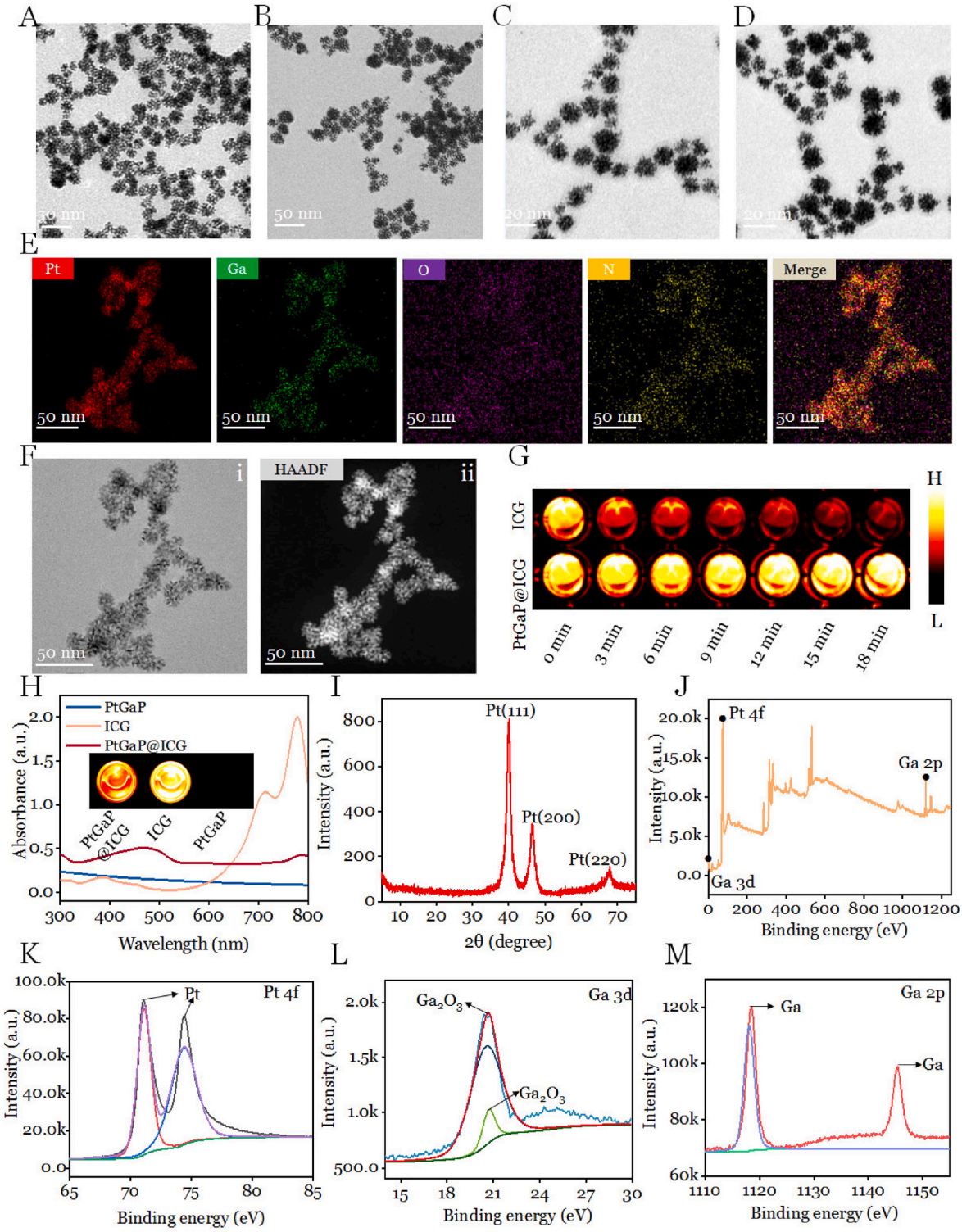

Fig. 2. TEM images of (A) PtGa and (B) PtGaP. HRTEM images of (C) PtGa and (D) PtGaP. (E) Elemental maps of Pt, Ga, O, N and their merged image, (F) HRTEM and (G) from PtGaP. (G) NIR-II fluorescent images of ICG (uplayer) and PtGaP@I (downlayer) with continuous 808 nm laser lighting for various minutes. (H) Absorption spectra and NIR-II luminescence images (inserted) of PtGa, ICG, and ICG PtGaP@I. (I) XRD spectrum of PtGaP. (J) Full XPS, high-resolution (K) Pt 4f, (L) Ga 3d and (M) Ga 2p spectra of PtGaP.

microscopy (TEM) image of PtGaP presents better dispersion with discernible morphology transformation (Fig. 2B). Size and zeta potential variation of PtGaP is studied by DLS after immersed with 0.9 % NaCl, serum, pH = 6.5 and pH = 7.4 buffers (Figs. S3 and S4). No changes in the positive charges on the surface of PtGaP are observed, confirming the superior stability of our nanomedicine. We are surprised to find that after incubation in a series of solvents for different durations, the size has not changed significantly, indicating that due to the encapsulation by PEG_{2000}, PtGaP has a relatively long blood retention time. Meanwhile, we prepare pure Pt and pure Ga nanocrystals using the same method and discover that a complete mesoporous morphology could also be achieved (Figs. S5 and S6). Therefore, it can be concluded that our method is a universal one for fabrication of mesoporous noble metal. Further, observing by magnified TEM and high-resolution TEM (HRTEM), an average diameter ~ 3 nm that make mesopores in the exteriors and interiors of each nanoparticle (Fig. 2C and D). According to previous work [55], these bimetallic nanoparticles are assembled by spatially interconnected arms. Latterly, the exact constituent elements

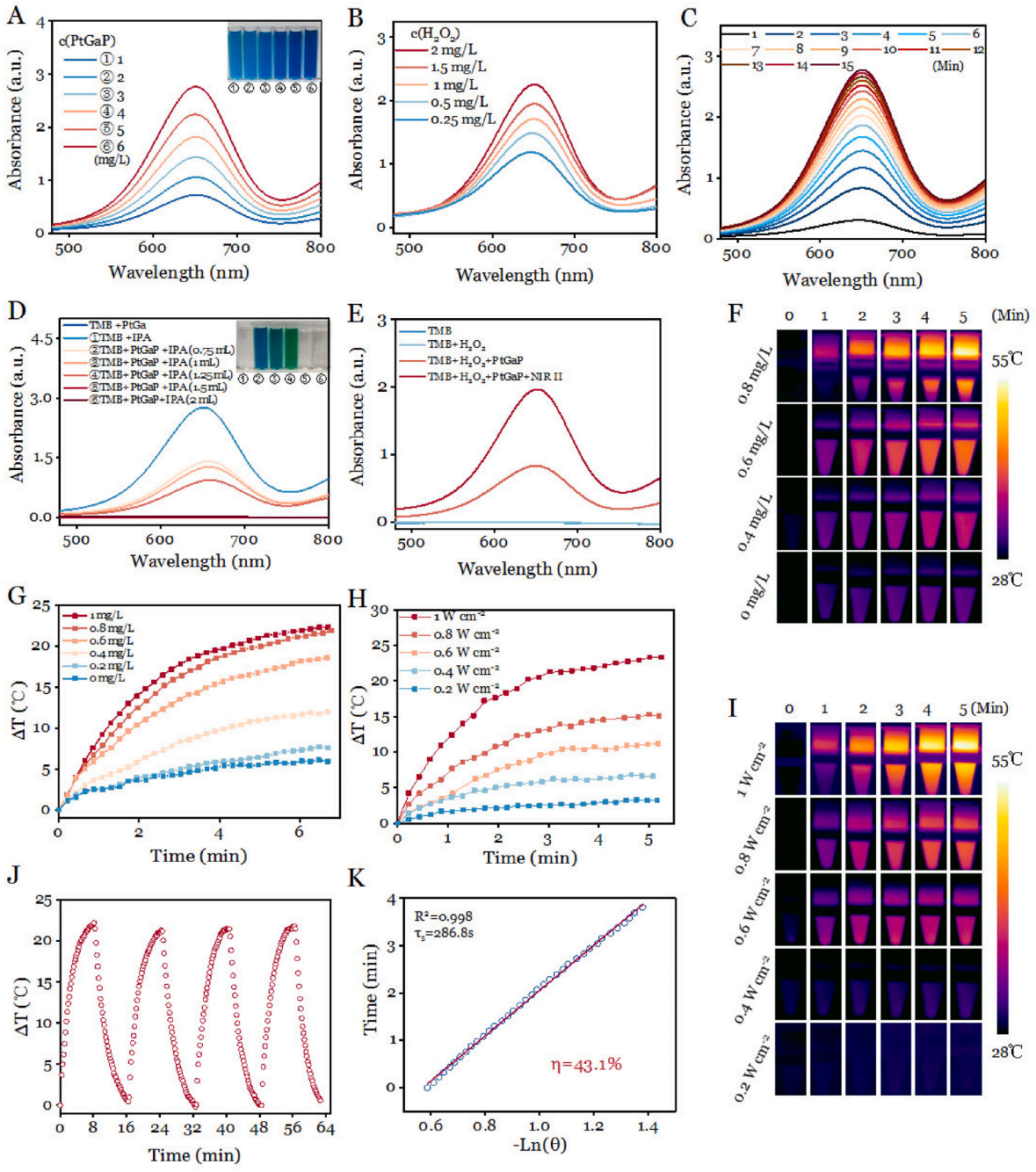

Fig. 3. (A) UV–*vis* absorption spectra and digital images showing the generated oxide TMB (inset) after incubating TMB with 0.5 mg/L H_2O_2 in the presence of varying concentrations of PtGaP. (B) Absorption spectra of oxide TMB following incubation with PtGaP (3 mg/L) and different H_2O_2 doses over various time periods. (C) UV–*vis* absorption spectra of oxide TMB after incubation with PtGaP (3 mg/L) and H_2O_2 (0.5 mg/L) for different durations. (D) UV–*vis* absorption spectra and digital images (inset) of oxide TMB after incubation with different formulations and various concentrations of IPA. (E) UV–*vis* absorption spectra of oxide TMB following different treatments. (F) IR thermal images and temperature change curves (G) of PtGaP at different concentrations, exposed to 1064 nm laser irradiation for 5 min. (H) Temperature change curves and (I) IR thermal images of PtGaP subjected to 1064 nm laser irradiation at varying power densities. (J) Temperature variations of PtGaP over four cycles of laser on/off. (K) Linear relationship between cooling time and -Ln(θ).

are further analyzed by energy dispersive spectrum that the mass fraction of Pt and Ga are 83.46 %, 11.33 %, respectively (Fig. S7). To further determine the exact content of Ga in PtGa, we perform acid digestion of this mesoporous nanoparticles and measure the concentrations of Ga and Pt using inductively coupled plasma optical emission spectrometer (ICP-OES). The results show that the ratio of Pt to Ga in the PtGa is approximately 9:1. The corresponded high-resolution scanning TEM (HR-STEM), high angle annular dark field microscope (HAADF) and elemental mapping images show that Ga, Pt, O is evenly scattered in the PtGaP nanoparticles (Fig. 2E and F). The successful preparation of PtGaP is validated *via* the characteristic peaks of PEG_{2000} in Fourier transform infrared (FTIR) spectra (Fig. S8). Thereafter, ICG molecules, as the fluorescent dye for labeling PtGaP both *in vitro* and *in vivo*, is successfully loaded in the stacked mesopores (PtGaP@I) and the loading efficiency is quantitatively determined to be 19.22 ± 2.03 % based on standard curve of ICG concentration. Evidently, the absorption peaks (780 nm) from ICG can be successfully detected in PtGaP@I, reflecting that it can be utilized for bioimaging contrast agent in NIR-II (Fig. 2M). The off-peak fluorescence beyond 1000 nm from ICG and PtGaP@I are recorded by a spectrofluorometer and bioimaging system with an InGaAs detector in NIR-II (1000–1700 nm) (Fig. 2H). Further, the photo-stabilities of ICG and PtGaP@I in water are subsequently measured by a NIR-II fluorescent bioimaging system. Inspiringly, free ICG lost ~92.3 % of its initial fluorescence intensity after continuous illumination for 18 min. By contrast, PtGaP@I fascinatingly retains almost 87.8 % of the initial signal intensity at the end of continuous irradiation (Fig. 3I and J). The data suggests that stacked mesopores could substantially stabilize ICG dye for preventing the quenching of water molecules, verifying that PtGaP@I can be further used as a NIR-II fluorescent contrast agent (Fig. 2G). The X-Ray Diffraction (XRD) diffraction peaks of PtGaP at 2θ = 39.9, 46.6 and 67.7° correspond to the indexed planes (111), (200) and (220) respectively, which were consistent with the fcc structure of platinum. In this study, we chose a 1064 nm laser primarily to achieve deeper tissue penetration and minimize tissue damage. Fortunately, Pt-based nanoparticles have surface plasmon resonance (SPR) effect. PtGa exhibits strong absorption within the range of 1000–1100 nm (Fig. S9), therefore, the free electrons on the surface undergo localized oscillations under 1064 nm laser irradiation, resulting in resonance that enhances laser absorption for NIR-II photothermal therapy. Owing to relatively low content of Ga, no diffraction peaks are found. Furthermore, X-ray photoelectron spectroscopy (XPS) is employed to investigate the valence states of the constituent elements. As shown in Fig. 2J, obviously the distinct Pt 4f, Ga 2p and Ga 3d peaks can be detected. From the full spectrum of XPS, we can see that the ratio of Ga^{III} to Ga^0 is 1:60. Such a high content of Ga^0 is very conducive to catalyze the generation of ROS. Apparently, the high-resolution Pt 4f XPS spectra displays two distinct peaks appear at 71.26 eV and 74.53 eV, which can be attributed to the formation of Pt metal (Fig. 2K). Both Gd 3d and Ga 2p spectra exhibit two binding energies, corresponding to the characteristic peaks of Ga_2O_3 and Ga mental, respectively (Fig. 2L and M). According to previous reports [56–58], pure gallium metal has a low melting point of 29.8 °C, and its strong affinity for oxygen causes it to readily form gallium oxide (Ga_2O_3), a high-melting point solid. This oxide layer can passivate the surface and stabilizing the surface structure. As a result, Ga-based liquid metal alloys are frequently observed to have surfaces predominantly composed of Ga_2O_3. Collectively, all above findings suggest that PtGaP nanoplatform with Fenton-like reaction, and NIR-II photothermal conversion capabilities are successfully developed.

3.2. Efficacious ROS generation and NIR-II PTT

Gallium-based ROS generation therapies include photodynamic therapy (PDT), sonodynamic therapy (SDT), radiation dynamic therapy (RDT), electrodynamic therapy (EDT), and chemodynamic therapy (CDT). Owing to the similarities of Ga^0 and Fe^0, *in vitro* •OH generation from mesoporous nanostructure of PtGaP is determined using 3,3,5,5-tetramethylbenzidine (TMB). The oxidation product of TMB (oxTMB) shows a strong absorption at 645 nm (blue color). The ROS generated efficiency shows a clear dose dependence on both PtGaP and H_2O_2 with distinct blue solution generation (Fig. 3A and B). Specifically, the reaction is very rapid, reaching its peak value in approximately 15 min (Fig. 3C). Isopropyl alcohol (IPA) is widely known as a scavenger for •OH, exhilaratingly, when PtGaP is combined with 2.0 mg/mL of H_2O_2, the absorbed peak of the generated oxTMB shows a clear IPA concentration dependent manner (Fig. 3D). In particularly, there is a 2.4-fold increase in •OH production from PtGaP + H_2O_2 plus 1064 nm laser shining group compared to the non-NIR-II laser control, strongly highlighting the potent synergistic ROS amplification of the nanocarriers in cytoplasm of cancer cells (Fig. 3E). The temperature rise profile of PtGaP under 1064 nm NIR-II laser exposure is measured using an IR camera. Compared to the pure H_2O group (0 μg/mL), which shows minimal temperature change, the temperature increase in PtGaP is found to be dependent on its concentration (Fig. 3F). Specifically, a 800 mg/mL PtGaP solution demonstrated a consistent temperature rise within 5 min of NIR-II laser irradiation, reaching a maximum temperature difference ($\triangle$T) of 22.3 °C, confirming PtGaP's rapid response to NIR-II light (Fig. 3G). To further investigate its response to the 1064 nm laser, different power densities are applied, revealing a significant temperature increase in the 200 mg/mL PtGa solution as the power density increased (Fig. 3H and I). Additionally, the NIR-II photothermal agent PtGaP exhibits excellent photostability across four laser on/off cycles (Fig. 3J). To quantitatively assess the laser-to-heat conversion efficiency (η), thermal changes during the heating/cooling cycle (laser on/off) are analyzed (Fig. 3K). Using the established formula, the calculated η for PtGaP is approximately 43.11 %. Although the value is slightly lower compared to the previously reported mesoporous carbon mesoporous dopamine, it is comparable to previously reported plasmonic Pt superstructures [59–61]. Collectively, these results highlight the potential of the mesoporous PtGa nanoplatform as a promising nanomedicine for NIR-II laser-induced photothermal enhancement of OXT.

3.3. Cell viability and intracellular ROS generation

In this work, the mesoporous PtGaP nanomedicine is developed for the first time, so we must evaluate its biocompatibility toward normal cells and tumor cells. Interestingly, we discover that as the concentration increased, the cytotoxicity toward 4T1 cells significantly enhanced at 12 h post-treatment of PtGaP. At a concentration of 100 μg/mL, the survival rate of 4T1 cells was only 39 %, while the survival rate of normal gastric mucosal epithelial cells (GES-1) is twice that of 4T1 cells (Fig. 4A). We also assess the toxicity of PtGaP in normal breast cells (MCF-10A). Interestingly, due to the lack of high concentrations of H_2O_2, when the PtGaP concentration is set to 100 μg/mL, MCF-10A cells still maintains 80 % viability (Fig. S10). This demonstrates the tumor cell-specific killing activity of our nanomedicine. Further, we are encouraged to investigate the cell killing effect of PtGaP, GaP and PtP against tumor cells (H_2O_2 pretreating) upon continuous NIR-II laser shining (5 min, 1 W/cm^2). As shown in Fig. 4B, the survival rates in the PtGaP + L groups are significantly lower compared to the PtGaP-only treated groups. Notably, at concentrations of 300 μg/mL and 400 μg/mL, only 27 % and 14 % of 4T1 cells remain alive, respectively. Particularly, 75 % of cells are alive in GaP + L group (100 μg/mL) that is originate from Fenton-like reaction (Fig. S11). Clearly, we find that the cell killing effect of PtGaP + L is significantly greater than the combined effect of GaP + L and PtP + L (Fig. S11), further proving the more efficient synergistic killing capability of PtGa-based nanomedicine plus 1064 nm laser shining *via* NIR-II driven OXT. To distinctly observe the intracellular distribution of PtGaP, we label this mesoporous nanostructure with FITC dye (Ex 488 nm, Em 550 nm). CLSM and flow cytometry are then employed to evaluate the cellular uptake efficiency of PtGaP by 4T1 cells. Notably, green signals in the cytoplasm increase over time, confirming a time-dependent endocytosis of PtGaP (Fig. 4F).

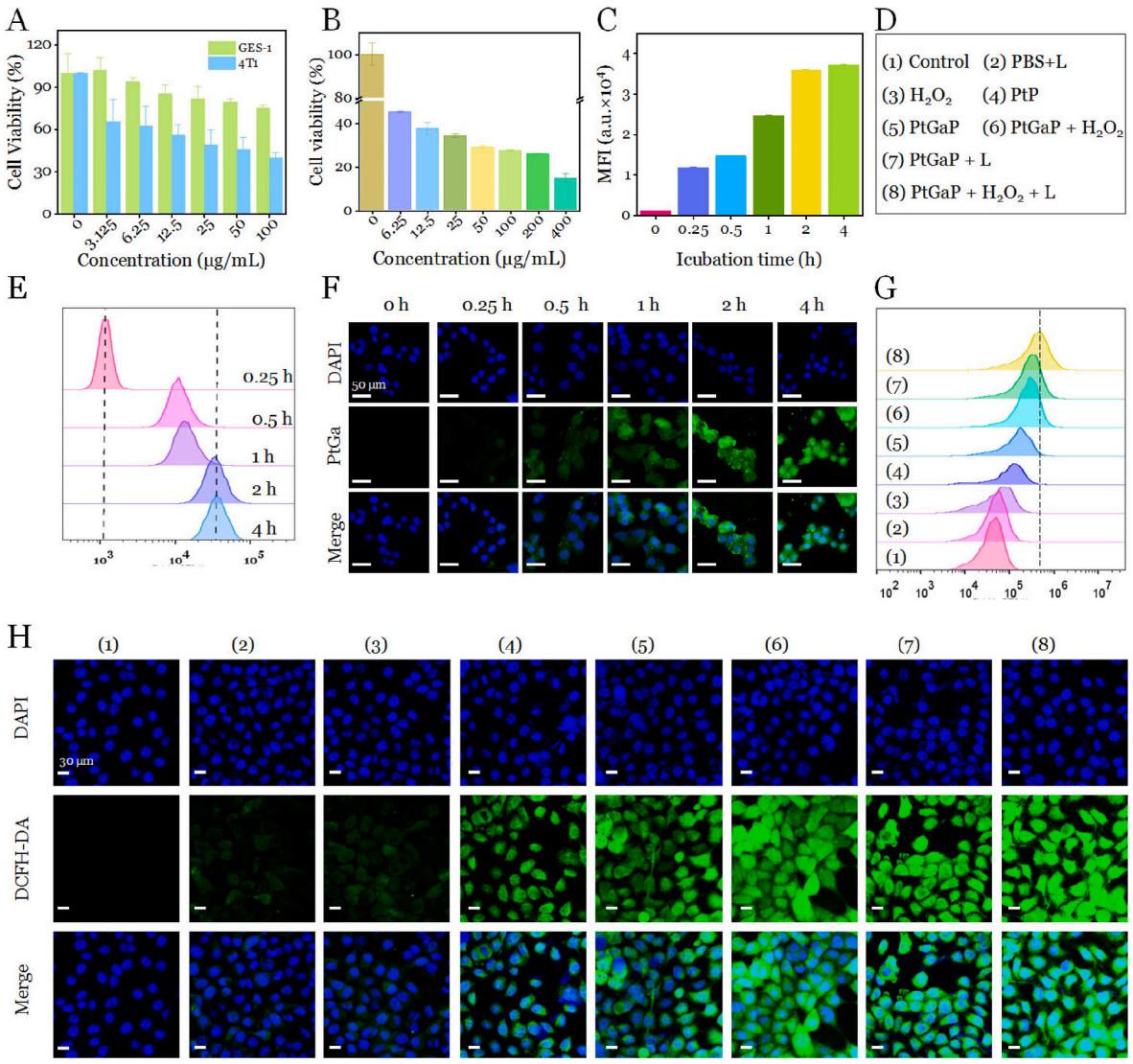

Fig. 4. (A) Cell viability of 4T1 and GES-1 cells following 12 h treatment with various concentrations of PtGaP. (B) Cell viability of 4T1 cells after treatment with PtGaP, NIR-II laser irradiation, and H_2O_2. (C) Mean fluorescence intensity in 4T1 cells after incubation with PtGaP for different durations. (D) Grouping of cells for ROS generation studies. (E) Flow cytometry and (F) CLSM analysis of 4T1 cells after incubation with PtGaP (labeled with FITC) for varying durations. (G) Flow cytometry and (H) CLSM analysis of cytoplasmic ROS levels in 4T1 cells after eight different treatments.

The flow cytometry results align with the CLSM observations, showing a similar time-dependent pattern, with endocytosis reaching saturation at 4 h (Fig. 4E and C). Furthermore, we are motivated to explore the potential mechanism underlying tumor cell destruction by qualitatively assessing intracellular ROS levels after 4 h of PtGaP incubation. Initially, 4T1 cells are randomly divided into eight groups (Fig. 4D). After various treatments, intracellular ROS production is measured using the commercially available indicator, 2′,7′-dichlorofluorescein diacetate (DCFH-DA, Ex 488 nm, Em 550 nm). The fluorescence intensity of the eight groups is then quantified using both flow cytometry and CLSM. As shown in Fig. 4G–S12, S13, fluorescence levels in the control and PBS + L groups are similar, while PtGaP-treated cells exhibit approximately four times higher ROS production. Notably, the cytoplasmic ROS levels in PtGaP + L-treated tumor cells pre-incubated with 100 μM H_2O_2 are 2.7 times higher than in the PtGaP-only group, strongly confirming the enhanced OXT effect in the tumor microenvironment under NIR-II laser irradiation. Additionally, dim intracellular green fluorescence is observed in the control and PBS groups, whereas a significantly higher green fluorescence is detected in the PtGaP + H_2O_2 group, highlighting the potent Fenton-like effect of our Ga-based nanomaterials (Fig. 4H). As anticipated, tumor cells treated with PtGaP + H_2O_2 plus 1064 nm laser illumination demonstrate the strongest green signal compared to the PtGaP + H_2O_2 and PtGaP + L groups (Fig. 4H). Collectively, these findings confirm that the novel PtGaP nanomedicine can be efficiently internalized by tumor cells, triggering cell death through robust ROS generation under NIR-II light irradiation and high H_2O_2 conditions.

Mitochondria are essential organelles, and their damage can directly trigger the intrinsic mitochondrial pathway of apoptosis. Various mitochondrial events can lead to cell apoptosis, including the release of caspase-activating protein cytochrome *c* (Cyto c), loss of mitochondrial membrane potential and depolarization, disruption of the electron transport chain, impaired oxidative phosphorylation, reduced ATP production, and interactions with pro-apoptotic Bax and anti-apoptotic Bcl-2 family proteins [62,63]. To investigate PtGaP-induced mitochondrial dysfunction, we first assess mitochondrial membrane potential using JC-1 staining (Fig. 5A and B). The JC-1 probe is known for detecting mitochondrial damage; in healthy mitochondria, JC-1 forms red J-aggregates, while in damaged mitochondria, it remains in its green monomeric form. A shift from red to green fluorescence indicates a loss of membrane potential and significant mitochondrial damage. After 4 h

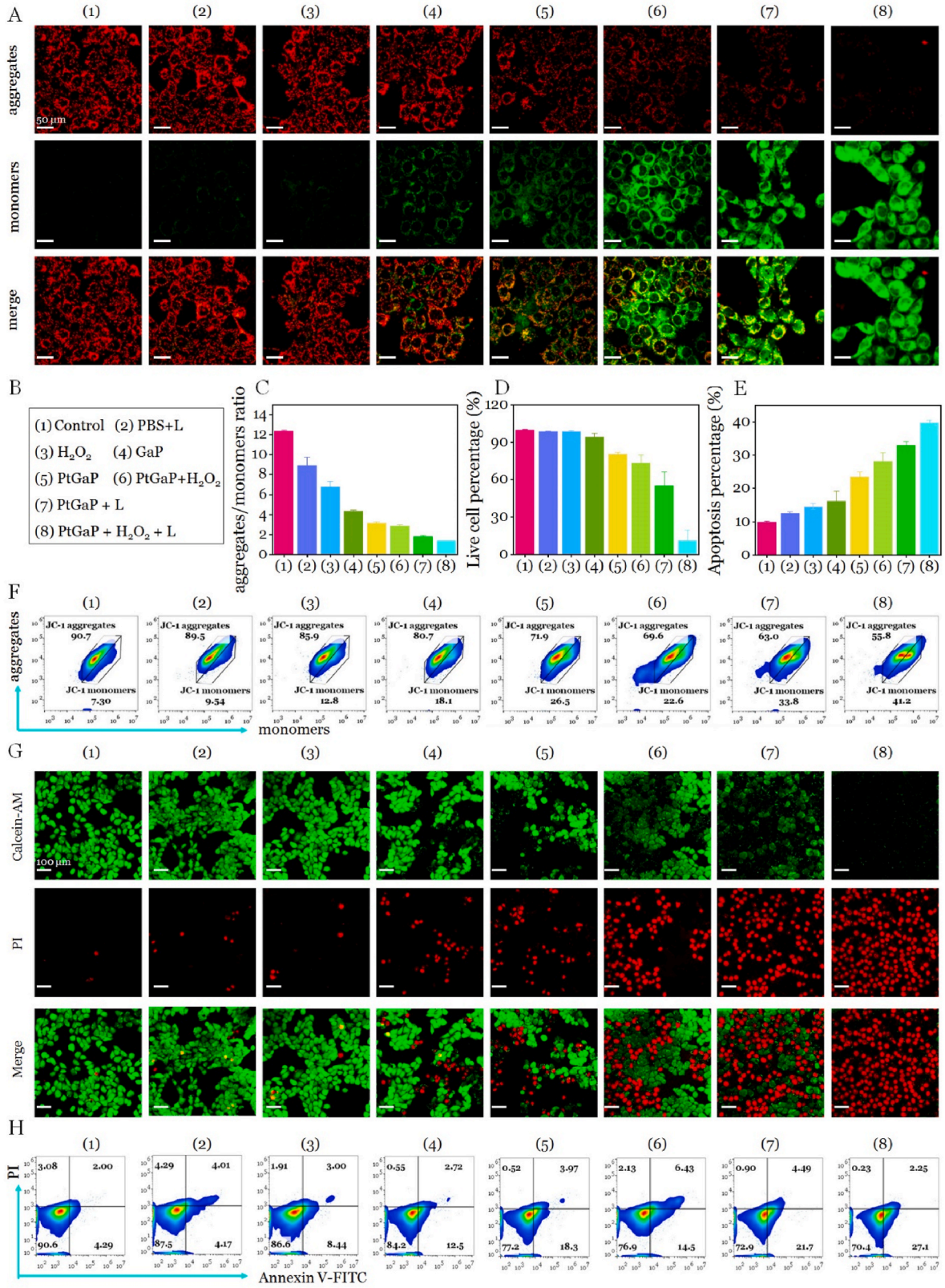

Fig. 5. (A) CLSM images of JC-1 stained 4T1 cells after eight different treatments. (B) Grouping of cells for JC-1 staining, CLSM imaging, and flow cytometry analysis. (C) Aggregate-to-monomer ratio in JC-1 stained 4T1 cells following various treatments. (D) Percentage of live cells in 4T1 cells after different treatments. (E) Apoptosis percentages in GES-1 cells after various treatments. (F) Flow cytometry analysis of JC-1 stained 4T1 cells after different treatments. (G) CLSM images of live/dead 4T1 cells after treatment with eight formulations. (H) Flow cytometry analysis of 4T1 cells following different treatments.

of incubation, 4T1 cells in the control, PBS, and H_2O_2 groups showed no significant green fluorescence (damaged mitochondria), with abundant red fluorescence (normal mitochondria). In contrast, treatment with PtP, PtGaP, and PtGaP + H_2O_2 results in the disappearance of red fluorescence and an increase in green fluorescence (monomers in the cytoplasm). Notably, the green signal in the PtGaP + L + H_2O_2 group is dramatically higher, indicating the most severe mitochondrial dysfunction, with a 2.5-fold decrease in the aggregate-to-monomer ratio compared to the PtGaP + H_2O_2 group (Fig. 5C). Further flow cytometry analysis of JC-1 stained 4T1 cells confirms mitochondrial-specific OXT-triggered damage (Fig. 5F). The aggregate-to-monomer ratio for mitochondrial membrane dysfunction in the PtGaP + H_2O_2 group with 1064 nm laser irradiation is 2.3 times higher than in the PtGaP + H_2O_2 group. These flow cytometry results align closely with the trends observed in CLSM imaging. Inspired by the significant cellular lethality observes in cell viability studies, green/red fluorescence for live/dead cell discrimination is captured using CLSM. As shown in Fig. 5D and G, no notable damage is detected in the PBS and laser-only groups. Excitingly, only 11 % of cells remains viable in the PtGaP + H_2O_2+L group, with a nearly 3.3-fold increase in dying cancer cells compared to the PtGaP + H_2O_2 group. This suggests that while pure OXT has some cell-eradicating capability, NIR-II PTT-induced OXT amplification significantly enhances cell death. Additionally, GES-1 cells treated with various conditions undergo double-staining with the calcein AM/PI assay. As expected, the apoptotic and necrotic rates are minimal (10 % and 12.5 %, respectively) in normal cells treated with PBS or laser alone, confirming that the basal power density of the 1064 nm laser does not harm normal tissue. Moreover, the apoptosis/necrosis analysis manifests that PtGaP induced a low mortality rate, with approximately 20 % apoptosis (Fig. 4E–H), further highlighting its excellent biocompatibility. All these findings demonstrate that the PtGaP-based nanoplatform, combined with laser irradiation, can specifically and

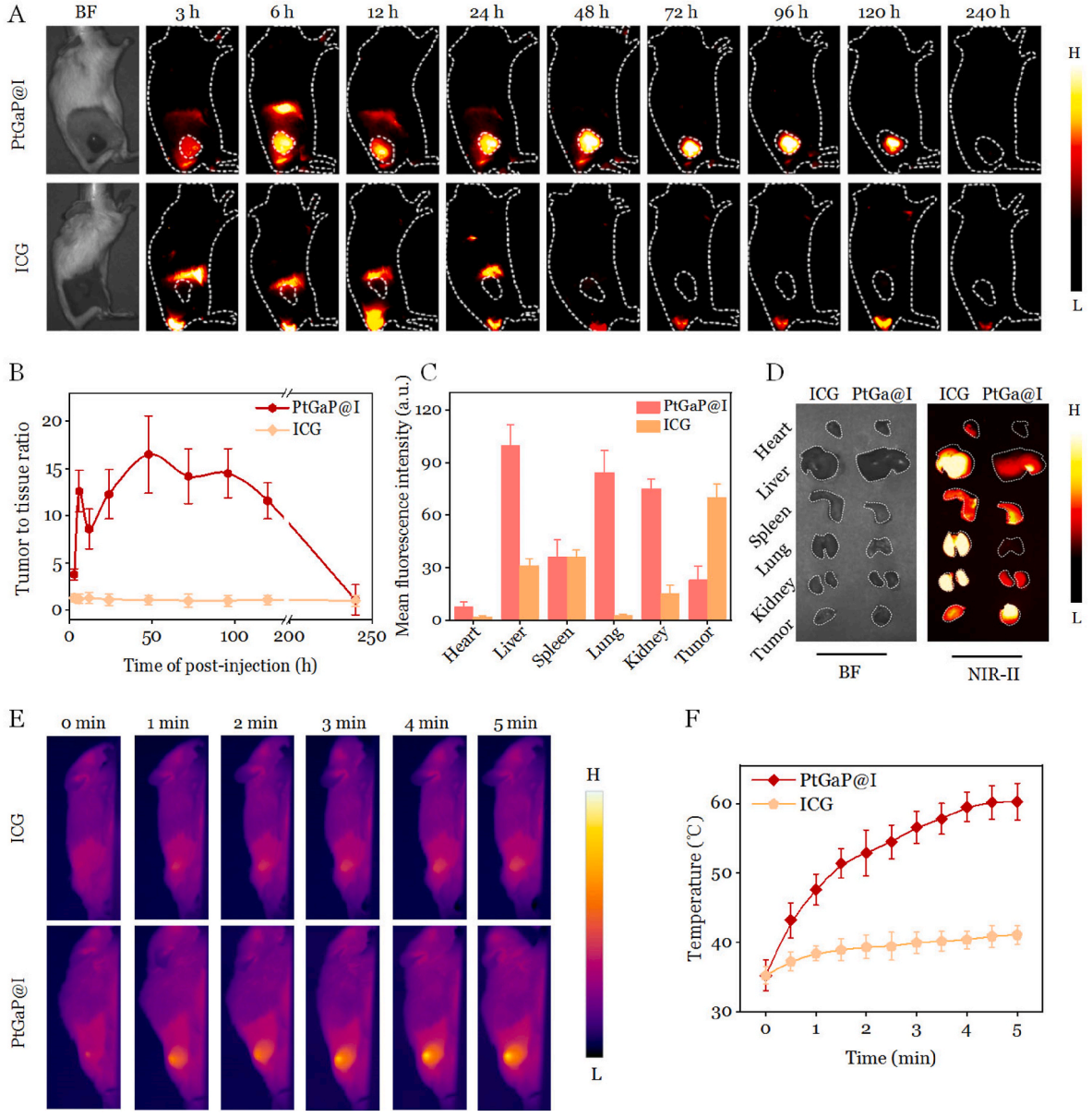

Fig. 6. (A) NIR-II fluorescence imaging of murine mammary tumor-bearing mice treated with PtGaP@I or ICG *via* intravenous injection at different time points. Tumor sites are marked by dotted circles. (B) TNR data derived from (A). (C) Quantitative fluorescent intensities and (D) *ex vivo* fluorescence images and of major organs and tumors collected from PtGaP@I and ICG-treated mice at 24 h post-injection. (E) Thermal images and (F) temperature increase curves of breast tumor-bearing mice 48 h post-injection of PtGaP@I or ICG, following 5 min of 1064 nm light exposure. Data are presented as mean ± standard deviation (mean ± SD, n = 5).

synergistically inhibit cancer cell proliferation under high H_2O_2 conditions, positioning PtGaP as a promising NIR-II PTT/OXT nanoagent for clinical breast cancer treatment.

3.4. In vivo tumor site recognition and NIR-II PTT evaluation

Inspired by the impressive *in vitro* tumor cell identification and theranostic potential of PtGaP, we aim to investigate the *in vivo* imaging behavior of this nanoplatform. Initially, the PtGaP-based nanoplatform is loaded with a NIR-II probe, indocyanine green (ICG, PtGaP@I), and its biodistribution and tumor targeting are evaluated in 4T1 murine mammary tumor-bearing Balb/C mice using NIR-II fluorescence imaging. As shown in Fig. 6A, following intravenous injection of free ICG or PtGaP@I, mice are imaged using a small animal imaging system (808 nm light excitation, 1000 nm long-pass filter). Fluorescent signals gradually accumulate at the tumor site, reaching their peak at 3 h post-injection. The tumor region (marked by a dotted circle) is clearly visible at 48 h, with signals gradually diminishing and becoming faint by 72 h. In contrast, the control group with free ICG displays negligible fluorescence at the tumor site, even after 240 h. As expected, the TNR in the PtGaP@I group is significantly higher than that in the ICG-only group (Fig. 6B). Notably, the highest TNR observed in the PtGaP@I group at 48 h post-injection, nearly 16.5 times greater than that of the ICG group. Furthermore, *ex vivo* NIR-II fluorescence imaging of organs and tumors at 24 h post-injection reveals that solid breast tumors from the PtGaP@I group manifest the highest tumor accumulation and the least uptake by reticuloendothelial system (RES) organs, compared to the ICG group (Fig. 6C and D). Excitingly, we also discover that after 120 h, almost no signal is observed in the liver and kidney areas (Fig. S14), demonstrating that the PtGaP can be rapidly metabolized and possess high biocompatibility. The 20−400 nm size range of these nanocarriers contributes to their passive targeting of tumors through the enhanced permeability and retention (EPR) effect. The larger surface area of the mesoporous morphology plays a key role in enhancing cell plasma membrane adhesion. Additionally, the EPR effect, couple with increased endocytosis facilitate by the unique nanostructure of PtGaP, significantly boosts tumor targeting and identification, with optimal results observes at 48 h post-injection. This time-point is therefore selected for early breast cancer diagnosis and photo-active therapy. Based on these findings, local tumor temperature is further measured from above two groups under 1064 nm light irradiation at 48 h post-injection of PtGaP@I and ICG, respectively. In the PtGaP@I group, the temperature rapidly increases, reaching a peak of approximately 60 °C after 5 min of continuous NIR-II irradiation. In contrast, the ICG-treated group only exhibited a temperature rise to ~41 °C under the same conditions (Fig. 6E and F). Due to the precise tumor targeting and minimal RES uptake, PtGaP@I nanomedicine alleviates concerns about potential systemic toxicity. While temperatures above 50 °C are effective for tumor ablation, they do not cause significant damage to surrounding normal tissues. In comparison to other Pt-based nanoparticles used for breast cancer treatment, our PtGaP nanoplatform, with its precise tumor accumulation, offers enhanced tumor diagnosis and effective synergistic therapy.

3.5. In vivo synergistic NIR-II PTT&OXT

Building on the promising *in vitro* cell-killing ability and exceptional tumor accumulation of our PtGaP-based nanoplatform, we have established a 4T1 tumor xenograft mouse model to further evaluate the *in vivo* synergistic therapeutic efficacy of NIR-II PTT/OXT with PtGaP. To test our therapeutic hypothesis, subcutaneous osteosarcoma-bearing mice are treated with four different formulations (PBS, PBS + L, PtGaP, PtGaP + L). As shown in Fig. 7A–D, tumor growth in the PBS and PBS+1064 nm laser-treated groups is rapid throughout the treatment period, indicating that 1064 nm laser (5 min, 1.0 W/cm^2) has minimal effect on tumor suppression. In contrast, treatment with PtGaP results in relatively better tumor growth inhibition, with both tumor volume and weight significantly controlled compared to the PBS group. Notably, tumors treated with PtGaP + L are nearly completely suppressed, exhibiting a remarkably lower tumor growth rate compared to the other groups (Fig. 7E). This enhanced eradication efficiency can be attributed to the synergistic effect of PTT-induced ROS amplification under 1064 nm light irradiation. Besides, in PtGaP + L treated mice, we observe significantly higher ROS level in tumor tissues in contrast with liver tissue (Fig. S15), demonstrating the specific capability of tumor cell killing. As a result, mice treated with PtGaP + L demonstrate a significant extension in survival, with over 90 % of the mice surviving beyond 100 days, whereas all PBS-treated mice are dead within 42 days (Fig. S16). Tumor tissues are also finally analyzed using H&E, TUNEL, and Ki67 staining. As shown in Fig. 7G, the H&E staining of the PtGaP + L group reveals the most condensed nuclear chromatin and the largest areas of necrotic tumor cells. Immunohistochemical analysis of TUNEL staining indicates a marked increase in apoptotic and necrotic cells in this group compared to the others. Additionally, the expression of Ki67, a widely recognized cell proliferation marker, is notably reduced in the PtGaP + L group, further confirming the superior tumor suppression achieved by our PtGaP-based PTT/OXT synergistic therapy under NIR-II light exposure. Body weight profiles from all groups illustrate minimal fluctuations, and no significant histopathological abnormalities are observed in the major organs of mice treated with PtGaP-based nanoplatforms and laser illumination (Fig. 7F–S17). Biochemical markers, such as those indicating liver and kidney function, show no significant changes after the administration of PtGaP + L for 1, 7, and 15 days (Fig. S18), providing strong evidence for the biosafety of this mesoporous nanomedicine. Further, the expression levels of interleukin (IL)-10 in five main organs are also conducted by immunohistochemical staining. Exhilaratingly, undiscernible fluorescent variation from IL-10 is detected in both PBS and PtGaP groups (Fig. S19). This data demonstrates that it has not activate immune activity in the system, demonstrating the high biosecurity of PtGaP. Long-term exposure to gallium compounds can potentially result in kidney damage and other health complications over time. Compared to the PBS group, we do not observe a significant increase in IL-10 expression after tail vein injection of GaP, indicating that gallium do not induce renal toxicity or an immune response (Fig. S20). Therefore, in this study, the doping of low amounts of gallium does not pose a toxicity problem. Collectively, these results highlight the excellent biocompatibility of PtGaP nanoplatform and its negligible systemic side effects.

4. Conclusion

In conclusion, we have successfully developed mesoporous PtGa nanoagents with a monodisperse diameter through a one-step solution-phase reaction. Thanks to this unique bimetallic alloy components, and following surface PEGylation, the PtGaP nanomedicine exhibits excellent NIR-II photothermal conversion properties from the Pt^0, alongside notable Fenton-like catalytic activity *via* the catalyst of Ga^0. With precise tumor cell targeting and the advantageous morphology, substantial ROS production is triggered by thermal activation upon NIR-II light irradiation. This results in a significant tumor cell-killing effect, both *in vitro* and *in vivo*, through a combination of OXT and PTT under 1064 nm light exposure. Our nanoplatform offers an innovative approach for synergistic OXT and NIR-II PTT to effectively inhibit malignant tumor growth.

CRediT authorship contribution statement

Yunfei Ying: Software, Methodology, Investigation, Formal analysis, Data curation. **Yonghui Su:** Validation, Software, Methodology, Formal analysis. **Ao Wang:** Software, Methodology. **Tingting Li:** Software, Investigation, Data curation. **Hongjun Zhuang:** Investigation, Data curation. **Siyaqi Li:** Software, Project administration, Formal analysis. **Xiaolong Liu:** Writing – review & editing, Software, Investigation, Formal analysis. **Kecan Lin:** Validation, Supervision, Software.

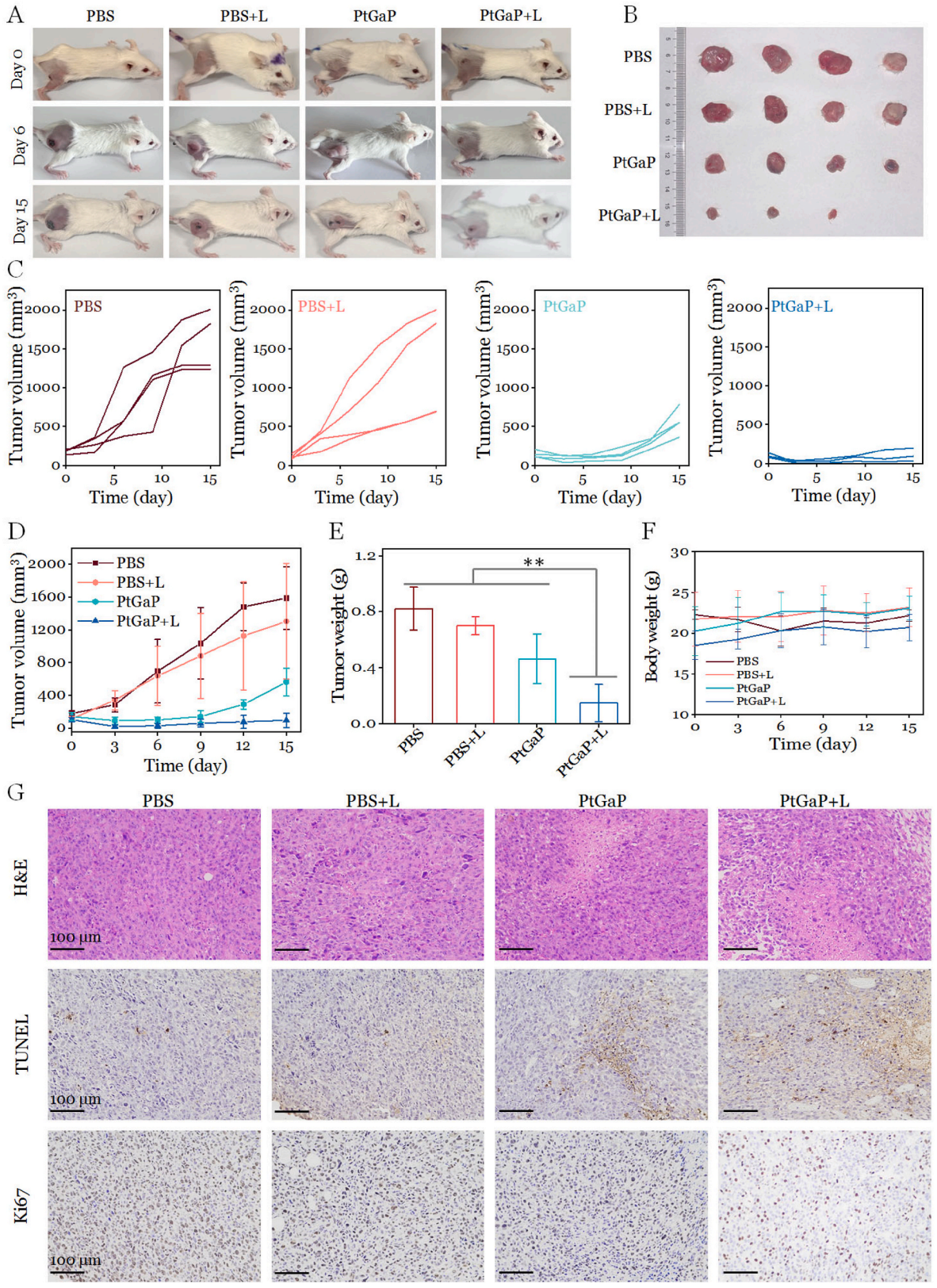

Fig. 7. (A) Representative digital images of breast cancer-bearing nude mice after 15 days of various treatments. (B) Images of the resected tumors from each treatment group after 15 days. (C) Individual tumor growth curves of mice treated with PBS, PBS + L, PtGaP, and PtGaP + L. (D) Tumor volume curves and (F) body weight changes following different treatments. (E) Weights of the resected tumors from various groups after 15 days of various treatments. (G) H&E, Ki67, and TUNEL staining of resected tumors after 15 days of various treatments. $^{**}p < 0.01$, with standard deviations (n = 4, mean ± SD).

Peiyuan Wang: Writing – review & editing, Writing – original draft, Validation, Supervision, Funding acquisition, Conceptualization. **Fuxing Zhang:** Writing – review & editing, Writing – original draft, Supervision, Funding acquisition, Formal analysis.

Declaration of competing interest

The authors declare that they have no known competing financial interests or personal relationships that could have appeared to influence the work reported in this paper.

Acknowledgement

This work was supported by the Natural Science Foundation of Fujian Province (2022J011283), the National Science Foundation for the Young Scientists of China (82303078, 82202326) and, the Medical-Engineering Integrated Guiding Project of Xiamen Science and Technology Bureau (3502Z20244ZD2007), and the Xiamen Public Hospital High Quality Development Project (XDFY-AW-2406-003, XYP2023001).

Appendix A. Supplementary data

Supplementary data to this article can be found online at https://doi.org/10.1016/j.mtbio.2025.101869.

Data availability

All experimental data within the article are available from the corresponding author upon reasonable request.

References

[1] R.L. Siegel, K.D. Miller, N.S. Wagle, A. Jemal, Cancer statistics, Ca - Cancer J. Clin. 73 (2023) (2023) 17–48.
[2] Z. Xie, Y. Huang, J. Wang, W. Guo, Y. Lin, Y. Lin, C. Du, Pt loaded CoFe2O4-based nanoparticles for breast cancer treatment with chemodynamic therapy and sonodynamic therapy, Cerm. Int. 51 (2025) 685–692.
[3] R.X. Hong, B.H. Xu, Breast cancer: an up-to-date review and future perspectives, Cancer Commun. 42 (2022) 913–936.
[4] J. Jayasekera, A.M.Y. Zhao, C. Schechter, K. Lowry, J.M. Yeh, M.D. Schwartz, S. O'Neill, K.J. Wernli, N. Stout, J. Mandelblatt, A.W. Kurian, C. Isaacs, Reassessing the benefits and harms of risk-reducing medication considering the persistent risk of breast cancer mortality in estrogen receptor-positive breast cancer, J. Clin. Oncol. 41 (2023) 859–870.
[5] E.J. Cathcart-Rake, A.J. Tevaarwerk, T.C. Haddad, S.D. D'Andre, K.J. Ruddy, Advances in the care of breast cancer survivors, BMJ Br. Med. J. (Clin. Res. Ed.) 382 (2023) e071565.
[6] S. Mahner, F. Trillsch, D. Chi, P. Harter, J. Pfisterer, F. Hilpert, A. Burges, T. Weissenbacher, A. du Bois, Neoadjuvant chemotherapy in ovarian cancer revisited, Ann. Oncol. 27 (2016) i30–i32.
[7] S. Loibl, P. Poortmans, M. Morrow, C. Denkert, G. Curigliano, Breast cancer, Lancet 397 (2021) 1750–1769.
[8] P. Chowdhury, U. Ghosh, K. Samanta, M. Jaggi, S.C. Chauhan, M.M. Yallapu, mBioactive nanotherapeutic trends to combat triple negative breast cancer, Bioact. Mater. 6 (2021) 3269–3287.
[9] Q.Q. Chen, M. Zhang, H. Huang, C.H. Dong, X.Y. Dai, G.Y. Feng, L. Lin, D.D. Sun, D. Y. Yang, L. Xie, Y. Chen, J. Guo, X.X. Jing, Single atom-doped nanosonosensitizers for mutually optimized sono/chemo-nanodynamic therapy of triple negative breast cancer, Adv. Sci. 10 (2023) 2206244.
[10] P. Tiwari, R.P. Shukla, K. Yadav, N. Singh, D. Marwaha, S. Gautam, A.K. Bakshi, N. Rai, A. Kumar, D. Sharma, P.R. Mishra, Dacarbazine-primed carbon quantum dots coated with breast cancer cell-derived exosomes for improved breast cancer therapy, J. Contr. Release 365 (2024) 43–59.
[11] F.D. Moghaddam, G. Heidari, E.N. Zare, E. Djatoubai, A.C. Paiva-Santos, F. R. Bertani, A.M. Wu, Carbohydrate polymer-based nanocomposites for breast cancer treatment, Carbohydr. Polym. 304 (2023) 120510.
[12] N. Wang, Q.Y. Zhang, Z.Y. Wang, Y.C. Liu, S. Yang, X.R. Zhao, J.Y. Peng, A chemo/chemodynamic nanoparticle based on hyaluronic acid induces ferroptosis and apoptosis for triple-negative breast cancer therapy, Carbohydr. Polym. 329 (2024) 121795.
[13] Y. Wang, J. Zhang, Y. Wang, J. Yu, Y. Gao, Y. Yang, X. Li, H. Wang, S. Li, A NIR-II-emissive organic nanomedicine with biomimetic engineering for high-contrast targeted bioimaging and multiple phototherapies of pancreatic tumors, Adv. Funct. Mater. 34 (2024) 2406483.
[14] K. Lee, Y. Gao, S. Chou, Y. Wan, A.C. Hsu, J. Tan, Y. Li, Z. Guan, H. Chen, S. Li, K. Wong, C. Lee, Construction of through-space charge-transfer nanoparticles for facilely realizing high-performance NIR-II cancer phototheranostics, Adv. Funct. Mater. 34 (2024) 2407317.
[15] R. Du, T. Li, Q. Wu, P. Wang, X. Yang, Y. Fan, Y. Qiu, K. Yan, P. Wang, Y. Zhao, W. W. Zhao, G. Chen, In situ engineering of the Cu^{+}/Cu^{0} interface to boost C_{2+} selectivity in CO_2 electroreduction, ACS Appl. Mater. Interfaces 14 (2022) 36527–36535.
[16] M. Mao, X. Ma, X. Wang, J. Ye, Microglial APOE4 promotes neuron degeneration in Alzheimer's disease through inhibition of lipid droplet autophagy, Acta Pharm. Sin. B 15 (2025) 657–660.
[17] T. Xu, X. Zhang, F. Liu, H. Guo, J. Zhang, S. Cai, D. Li, Y. Zhang, Y. Guan, W. Yu, D. Zou, L. Xiao, C. Wu, Reducing exciton binding energy of antimony-based perovskites by improving the phase purity for efficient solar cells, Mater. Horiz. (2025), https://doi.org/10.1039/D5MH00003C.
[18] H. Chen, Y. Wang, X. Cui, S. Li, C. Lee, Recent advances in hypoxia-overcoming strategy of aggregation-induced emission photosensitizers for efficient photodynamic therapy, Adv. Healthcare Mater. 10 (2021) 202101607.
[19] J. Deng, D. Xian, X. Cai, S. Liao, S. Lei, F. Han, Y. An, Q. He, G. Quan, C. Wu, T. Peng, C. Lu, H. Zhang, Surface-EngineeredVanadium carbide MXenzyme for anti-inflammation and photo enhanced antitumor therapy of colon diseases, Adv. Funct. Mater. 33 (2023) 2211846.
[20] J. Yao, Y. Qiu, J. Xing, Z. Li, A. Zhang, K. Tu, M. Peng, X. Wu, F. Yang, A. Wu, Highly-efficient gallium-interference tumor therapy mediated by gallium-enriched prussian blue nanomedicine, ACS Nano 18 (2024) 5556–5570.
[21] S.V. Torti, F.M. Torti, Iron and cancer: more ore to be mined, Nat. Rev. Cancer 13 (2013) 342–355.
[22] K.L. Feldenzer, J. Sarno, Hypercalcemia of malignancy, J. Adv. Pract. Oncol. 9 (2018) 496–504.
[23] C. Bonchi, F. Imperi, F. Minandri, P. Visca, E. Frangipani, Repurposing of gallium-based drugs for antibacterial therapy, Biofactors 40 (2014) 303–312.
[24] J. He, Y. Ye, D. Zhang, K. Yao, M. Zhou, Visualized gallium/lyticase-integrated antifungal strategy for fungal keratitis treatment, Adv. Mater. 34 (2022) 2206437.
[25] V.K. Truong, A. Hayles, R. Bright, T.Q. Luu, M.D. Dickey, K. Kalantar-Zadeh, K. Vasilev, Gallium liquid metal: nanotoolbox for antimicrobial applications, ACS Nano 17 (2023) 14406–14423.
[26] J. Connelly, C. Zoss, K. Schmainda, M. Al-Gizawiy, F.S. Pinheiro, C. Chitambar, CTNI-57. Preliminary results of a phase 1 trial of oral gallium maltolate in recurrent glioblastoma, Neuro Oncol. 25 (2023) 89.
[27] D.P. Kelsen, N. Alcock, S. Yeh, J. Brown, C. Young, Pharmacokinetics of gallium nitrate in man, Cancer 46 (1980) 2009–2013.
[28] I.H. Krakoff, R.A. Newman, R.S. Goldberg, Clinical toxicologic and pharmacologic studies of gallium nitrate, Cancer 44 (1979) 1722–1727.
[29] T. Xie, Y. Qi, Y. Li, F. Zhang, W. Li, D. Zhong, Z. Tang, M. Zhou, Ultrasmall Ga-ICG nanoparticles based gallium ion/photodynamic synergistic therapy to eradicate biofilms and against drug-resistant bacterial liver abscess, Bioact. Mater. 6 (2021) 3812–3823.
[30] Y.H. Liu, G. Wang, R.J. Wang, D.Q. Zhao, M.X. Pan, W.H. Wang, Super plastic bulk metallic glasses at room temperature, Science 315 (2007) 1385–1388.
[31] M.D. Demetriou, M.E. Launey, G. Garrett, J.P. Schramm, D.C. Hofmann, W. L. Johnson, R.O. Ritchie, A damage-tolerant glass, Nat. Mater. 10 (2011) 123–128.
[32] C. Zhang, W. Bu, D. Ni, S. Zhang, Q. Li, Z. Yao, J. Zhang, H. Yao, Z. Wang, J. Shi, Synthesis of iron nanometallic glasses and their application in cancer therapy by a localized Fenton reaction, Angew. Chem. Int. Ed. 55 (2016) 2101–2106.
[33] Z. Tang, H. Zhang, Y. Liu, D. Ni, H. Zhang, J. Zhang, Z. Yao, M. He, J. Shi, W. Bo, Antiferromagnetic pyrite as the tumor microenvironment-mediated nanoplatform for self-enhanced tumor imaging and therapy, Adv. Mater. 29 (2017) 1701683.
[34] M.R. Younis, C. Wang, R. An, S. Wang, M.A. Younis, Z.Q. Li, Y. Wang, A. Ihsan, D. Ye, X.H. Xia, Low power single laser activated synergistic cancer phototherapy using photosensitizer functionalized dual plasmonic photothermal nanoagents, ACS Nano 13 (2019) 2544–2557.
[35] K. Hu, P. Zhou, Y. Yang, T. Hall, G. Nie, Y. Yao, X. Duan, S. Wang, Degradation of microplastics by a thermal Fenton reaction, ACS EST Engg. 2 (2022) 110–120.
[36] D. Xu, Y. Li, S. Yin, F. Huang, Strategies to address key challenges of metallacycle/metallacage-based supramolecular coordination complexes in biomedical applications, Chem. Soc. Rev. 53 (2024) 3167–3204.
[37] Y. Li, F. Huang, P.J. Stang, S. Yin, Supramolecular coordination complexes for synergistic cancer therapy, Acc. Chem. Res. 57 (2024) 1174–1187.
[38] Q. Yu, J. Li, Y. Yu, M. Yan, D. Xu, S. Yin, Biomarker-activatable photosensitizers with aggregation-induced emission characteristics for photodynamic therapy, Coord. Chem. Rev. 518 (2024) 216056.
[39] Y. Li, M. Jiang, M. Yan, J. Ye, Y. Li, W. Dehaen, S. Yin, Near-infrared boron–dipyrrin (BODIPY) nanomaterials: molecular design and anti-tumor therapeutics, Coord. Chem. Rev. 506 (2024) 215718.
[40] X. Lin, F. Chen, X. Yu, H. Wang, H. Qiu, Y. Li, S. Yin, P.J. Stang, Phenylthiol-BODIPY-based supramolecular metallacycles for synergistic tumor chemo-photodynamic therapy, Proc. Natl. Acad. Sci. U.S.A 119 (2022) e2203994119.
[41] J. Li, H. Tian, F. Zhu, S. Jiang, M. He, Y. Li, Q. Luo, W. Sun, X. Liu, P. Wang, Amorphous ultra-small Fe-based nanocluster engineered and ICG loaded organo-mesoporous silica for GSH depletion and photothermal-chemodynamic synergistic therapy, Adv. Healthcare Mater. 11 (2022) 2201986.
[42] Q. Meng, W. Wang, H. Wang, Y. Tao, N. Anastassova, T. Sun, Y. Sun, L. Wang, Photothermal and enhanced chemodynamic reinforced anti-tumor therapy based on PDA@POM nanocomposites, J. Colloid Interface Sci. 678 Part C (2025) 796–803.
[43] W. Kang, Y. Wang, L. Xin, L. Chen, K. Zhao, L. Yu, X. Song, Z. Zheng, R. Dai, W. Zhang, R. Zhang, Biodegradable cascade-amplified nanotheranostics for

photoacoustic-guided synergistic PTT/CDT/starvation antitumor in the NIR-II window, Adv. Healthcare Mater. 13 (2024) e2401459.
[44] K. Wei, Y. Wu, X. Zheng, L. Ouyang, G. Ma, C. Ji, M. Yin, A light-triggered J-aggregation-regulated therapy conversion: from photodynamic/photothermal therapy to long-lasting chemodynamic therapy for effective tumor ablation, Angew. Chem. Int. Ed. 63 (2024) e202404395.
[45] S. Feng, Y. Xiao, J. Lu, Z. Chen, Z. Jiang, Q. Xu, W. Gu, S. Wang, Q. Zhao, Tumor microenvironment sensitization via dual-catalysis of carbon-based nanoenzyme for enhanced photodynamic therapy, J. Colloid Interface Sci. 663 (2024) 577–590.
[46] Y. Yang, Q. Xu, W. Gu, K. Nan, S. Chen, S. Wang, J. Zhang, Q. Zhao, Oxidative stress-augmented Cu-doped hollow mesoporous carbon nanozyme for photothermal/photodynamic synergistic therapy, J. Colloid Interface Sci. 683 (2025) 910–925.
[47] J. Lu, L. Song, S. Feng, K. Wang, Y. Mao, Y. Gao, Q. Zhao, S. Wang, Nanozyme-mediated biocatalysis as a mitochondrial oxidative stress amplifier for tumor nanocatalytic immunotherapy, Chem. Eng. J. 481 (2024) 148270.
[48] C. Wang, L. Zhou, C. Liu, J. Qiao, X. Han, L. Wang, Y. Liu, Q. Qiu, Z. Zhang, J. Wang, X. Zhou, M. Zeng, L. Yu, L. Fu, Pt nanoshells with a high NIR-II photothermal conversion efficiency mediates multimodal neuromodulation against ventricular arrhythmias, Nat. Commun. 15 (2024) 6362.
[49] D. Lee, S. Khaja, J.C. Velasquez-Castano, M. Dasari, C. Sun, J. Petros, W.R. Taylor, N. Murthy, Synthesis of iron nanometallic glasses and their application in cancer therapy by a localized Fenton reaction, Nat. Mater. 6 (2007) 765–769.
[50] J. Zhang, X. Xu, H. Wei, D. Wu, L. Zeng, Pt/Pd dual-modified porphyrin metal-organic frameworks for NIR-II photothermal-enhanced photodynamic/catalytic therapy, J. Colloid Interface Sci. 678 (Part A) (2025) 42–52.
[51] N. Zhang, C. Han, Y.J. Xu, J.J. Foley IV, D. Zhang, J. Codrington, S.K. Gray, Y. Sun, Near-field dielectric scattering promotes optical absorption by platinum nanoparticles, Nat. Photonics 10 (2016) 473–482.
[52] Y. Zhu, Z. Wang, R. Zhao, Y. Zhou, L. Feng, S. Gai, P. Yang, Pt decorated $Ti_3C_2T_x$ MXene with NIR-II light amplified nanozyme catalytic activity for efficient phototheranostics, ACS Nano 16 (2022) 3105–3118.
[53] M. Manikandan, N. Hasan, H.F. Wu, Platinum nanoparticles for the photothermal treatment of Neuro 2A cancer cells, Biomaterials 34 (2013) 5833–5842.
[54] Q. Li, L. Liu, H. Huo, L. Su, Y. Wu, H. Lin, X. Ge, J. Mu, X. Zhang, L. Zheng, J. Song, Nanosized janus AuNR-Pt motor for enhancing NIR-II photoacoustic imaging of deep tumor and Pt^{2+} ion-based chemotherapy, ACS Nano 16 (2022) 7947–7960.
[55] K. Eid, H. Wang, P. He, K. Wang, T. Ahamad, S.M. Alshehri, Y. Yamauchi, L. Wang, One-step synthesis of porous bimetallic PtCu nanocrystals with high electrocatalytic activity for methanol oxidation reaction, Nanoscale 7 (2015) 16860.
[56] Y. Takano, Y. Hayashi, J. Fukushima, H. Takizawa, Room-temperature synthesis of γ-Ga_2O_3 nanoparticles from galliummetal *via* ultrasound irradiation, Adv. Powder Technol. 32 (2021) 860–865.
[57] T.E. Hsieh, J. Frisch, R.G. Wilks, M. Bär, Unravelling the surface oxidation-induced evolution of the electronic structure of gallium, ACS Appl. Mater. Interfaces 15 (40) (2023) 47725–47732.
[58] H. Wittkämper, S. Maisel, M. Wu, J. Frisch, R.G. Wilks, M. Grabau, E. Spiecker, M. Bär, A. Görling, H.P. Steinrück, C. Papp, Oxidation induced restructuring of Rh-Ga SCALMS model catalyst systems, J. Chem. Phys. 153 (2020) 104702.
[59] S. Feng, Y. Mao, X. Wang, M. Zhou, H. Lu, Q. Zhao, S. Wang, Triple stimuli-responsive ZnO quantum dots-conjugated hollow mesoporous carbon nanoplatform for NIR-induced dual model antitumor therapy, J. Colloid Interface Sci. 559 (2020) 51–64.
[60] H. Cheng, Y. He, J. Lu, Z. Yan, L. Song, Y. Mao, D. Di, Y. Gao, Q. Zhao, S. Wang, Degradable iron-rich mesoporous dopamine as a dual-glutathione depletion nanoplatform for photothermal-enhanced ferroptosis and chemodynamic therapy, J. Colloid Interface Sci. 639 (2023) 249–262.
[61] Q. Wang, H. Wang, Y. Yang, L. Jin, Y. Wang, X. Yan, J. Wu, R. Gao, P. Lei, J. Zhu, Y. Wang, S. Song, H. Zhang, Plasmonic Pt superstructures with boosted near-infrared absorption and photothermal conversion efficiency in the second biowindow for cancer therapy, Adv. Mater. 31 (2019) 1904836.
[62] A. Shah, M.A. Dobrovoskaia, Detection of nanoparticle-mediated change in mitochondrial membrane potential in T cells using JC-1 dye, Methods Mol. Biol. 2789 (2024) 153–159.
[63] D.F. Carrageta, L.F. Brito, P.F. Oliveira, M.G. Alves, Evaluation of human spermatozoa mitochondrial membrane potential using the JC-1 dye, Curr. Protoc. 2 (2022) e531.